condensed matter

MDPI

Article

Engineering Porous Silicon Nanowires with Tuneable Electronic Properties

S. Javad Rezvani [1,2,3,*], Nicola Pinto [1], Roberto Gunnella [1], Alessandro D'Elia [3], Augusto Marcelli [2,4] and Andrea Di Cicco [1]

1 School of science and technology, Physics division, University of Camerino, Via Madonna delle Carceri 9, 62032 Camerino, Italy; nicola.pinto@unicam.it (N.P.); roberto.gunnella@unicam.it (R.G.); andrea.dicicco@unicam.it (A.D.C.)
2 Istituto Nazionale di Fisica Nucleare - Laboratori Nazionali di Fisica Nucleare, Via Enrico Fermi 54, 00044 Frascati, Italy; augusto.marcelli@lnf.infn.it
3 Consiglio Nazionale delle Ricerche (IOM), Edificio Q2, Area Science Park, Strada Statale 14, km 163,5, 34149 Basovizza, Italy; delia@iom.cnr.it
4 International Centre for Material Science Superstripes, RICMASS, via dei Sabelli 119A, 00185 Rome, Italy
* Correspondence: rezvani@lnf.infn.it

Received: 4 August 2020; Accepted: 24 September 2020; Published: 28 September 2020

Abstract: Structural and electronic properties of silicon nanowires with pre-designed structures are investigated. Wires with distinct structure were investigated via advanced spectroscopic techniques such as X-ray absorption spectroscopy and Raman scattering as well as transport measurements. We show that wire structures can be engineered with metal assisted etching fabrication process via the catalytic solution ratios as well as changing doping type and level. In this way unique well-defined electronic configurations and density of states are obtained in the synthesized wires leading to different charge carrier and phonon dynamics in addition to photoluminescence modulations. We demonstrate that the electronic properties of these structures depend by the final geometry of these systems as determined by the synthesis process. These wires are characterized by a large internal surface and a modulated DOS with a significantly high number of surface states within the band structure. The results improve the understanding of the different electronic structures of these semiconducting nanowires opening new possibilities of future advanced device designs.

Keywords: nanowires; semiconductors; Raman; electronic structure; X-ray absorption spectroscopy

1. Introduction

In recent years, semiconducting nanowires (NWs), especially silicon-based ones, have been extensively characterized and considered for different applications. Their unique chemical and physical properties and their ideal compatibility with the state-of-the-art Si electronics makes them a suitable candidate for applications in nano-electronics, opto-electronics, solar cells and sensors, in particular to exploit quantum confinement phenomena and its effect on the modulation of the electronic configuration [1–4]. Porous silicon nanowires (PSNs) have recently triggered attention for their intense visible photoluminescence due to a strong quantum confinement within the pores [1,5]. However, electronic transport properties in these semi-insulating materials limit the electro-luminescence efficiency [6]. PSNs can also be used in optics and electro-optics due to their tunable refractive index and high internal surface [7,8]. Si nanowires are also promising candidates for one-dimensional superconductor-semiconductor hybrid systems, being optimal platforms for realizing Majorana zero modes [9,10]. The production of condensed matter Majorana zero modes is one of the building blocks of topological quantum computers. Furthermore, nanostructures have shown to be promising candidates in several applications from energy storage to superconductive devices [11–14], and Si

nanowires can be exploited in such applications as well. However, electronic properties of silicon nanowires are strongly dependent on their surface and core structures that can modify their electronic and physical-chemical properties.

Crystalline semiconducting nanowires are mainly grown using ultra high vacuum systems via vapor liquid solid (VLS) mechanism by chemical vapor deposition or via diffusion induced VLS in molecular beam epitaxy. On the other hand, porous silicon nanowires are usually produced via metal assisted catalytic etching (MAcE) [15,16]. In both cases, synthesized nanowires are usually doped due either to the doped substrate in the MAcE approach or by contamination via liquid metal droplet adatoms in the VLS method [17,18]. Recent researches using the VLS approach shows that single Ge crystalline wires could be achieved with particular geometries by the adatom flux dynamics modulation as a function of growth temperature [19,20]. It was previously shown that in MAcE process, silicon nanowires with pre-designed structures can be achieved via modulation of the etching mechanism by the metal and catalytic solution used and the substrate doping type and level [15]. However, the electronic structure and properties of fabricated wires are neither completely investigated nor understood. For instance, in doped semiconductors the conventional compensation is established by the addition of a substituting counter-dopant impurity to the doped crystal lattice. However, the compensation mechanism in geometrically confined systems can results in strong correlated electron interactions and formation of Columbic gaps [18]. Accordingly, a detailed investigation of the electronic structure properties based on their geometries and crystalline structures with their possible effects is mandatory.

Here, we have investigated structural and electronic properties of doped Si nanowires fabricated by the MAcE process with distinct structures. We show that the fabrication process leads to different wire structures based on the doping type and the level of the employed substrate as well as the etching recipe. The different structure of the wires results in different dominant single electronic configuration and density of state significantly dependent on the geometry of the wires. This leads in these systems to the observation of phonon scattering modulations and to a characteristic transport mechanism. The results may lead to the synthesis of wires with pre-designed structural and electronic properties to be used in devices with advanced designs.

2. Experimental

The silicon nanowires were fabricated by metal assisted chemical etching using colloidal lithography with a lateral resolution of a few nanometers. Si(100) substrates have been used, with four different p-(B doped) and n-(P-doped) doping level, with resistivity of $10 \div 30\ \Omega$cm and $0.01 \div 0.02\ \Omega$cm, respectively. The substrates were first cleaned in acetone and deionized water, then dipped in 10% HF solution to remove native oxide. The polystyrene nanospheres, synthesized by emulsion polymerization, with initial size of 140 nm, were deposited on the substrate (see Figure 1). The plasma etching was used subsequently for size reduction to a mean value of 90 nm, by a gas mixture of O_2 and Ar. In the next step, an Au layer of 20 nm thick was evaporated by an electron beam gun to be used as metal catalyst. Later, the nanospheres were removed by sonication in deionized water resulting in on ordered pattern on the substrate, followed by dipping of the sample in a solution of $HF:H_2O_2:H_2O$, using 50% HF and 30% H_2O_2 for six minutes. The MAcE process was performed at room temperature and in the dark to avoid contribution of photo-generated charge carriers to the etching process.

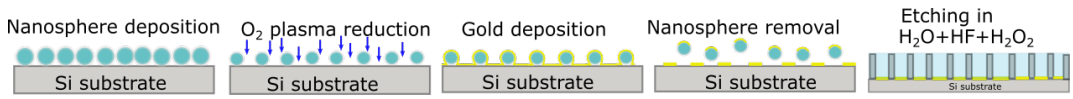

Figure 1. Layout of the multistage colloidal lithography. The polystyrene nanospheres with initial size of 140 nm, were deposited on the substrate. The plasma etching was used subsequently to reduce the size to a mean value of 90 nm, by a gas mixture of O_2 and Ar. An Au layer of 20 nm thick was evaporated. Finally, the nanospheres were removed by sonication in deionized water. The patterned structure then is etched in the catalytic solution for the fabrication of the nanowires.

The X-ray absorption spectroscopy were carried out at Si L- and O K-edge at the (IOM-CNR) BEAR beam-line at the Elettra synchrotron radiation center (Trieste, Italy) [21]. The Elettra beam energy was 2 GeV with a typical current of 300 mA. The beam-line operates in the 2.8÷1600 eV (443–0.775 nm) spectral region, delivering an intense photon beam of selectable ellipticity. The basic optical layout is based on the PMGM (Plane Mirror Grating Mirror) configuration. The beam-line exploits three monochromators for different energy range (i.e., normal-incidence GNIM from 2.7÷50 eV, grazing incidence G1200 for 40÷1200 eV and G1800 for 600÷1600 eV). In the present work, we have used only the G1200 monochromator of the grazing incidence channel, delivering typically a flux of $\sim 10^{11}$ photons/s (at 100 eV) with an energy resolution of 0.2 eV. The energy calibration was performed based on the $\pi - \pi^*$ transition of the C K-edge.

The charge transport measurements were carried out at SuperNanoLab at the University of Camerino. For DC electrical characterization, NWs were cooled down in a He closed cycle cryostat keeping samples immersed in the He gas. Resistivity and current-voltage (I–V) characteristics were measured as a function of the temperature, from about 10 K to 300 K, by a Picoammeter (Keithley mod. 6487), operating in the V/I mode (i.e., applying a constant voltage and measuring the current). The measurements were carried out in dark. The temperature was kept constant within 0.1 K, by an Eurotherm mod. 3216 temperature controller. A two contacts geometry was used for the electrical characterization.

Raman spectra were collected at the INFN-LNF laboratories using the Jasco NRS-5100 confocal Raman microscope, equipped with a 523 nm (green) laser with a 100x magnification objective. Exposure time for laser illumination was set to 10 s and spectra were collected 10 times for each point of measure and then averaged. Laser power was set to 10 mW to obtain maximum signal and high S/N ratio. The possible local damages were checked by presence of shift in the Raman peaks vs time and visible beam damages. No local damages of the samples were detected with this laser power and exposure time.

3. Results and Discussion

MAcE fabricated silicon nanowires have shown fabrication dependent morphology based on the etching solutions, metal used in the process and the doping type and level (more information can be found in Ref [15]). An example of scanning electron microscopy (SEM) of p-doped silicon nanowires fabricated via MAcE is shown in Figure 2. The wires are perpendicularly positioned in reference to the substrate. All samples exhibit similar topography with lengths distributions between 2–10 μm depending on the etching time. The diameters of the fabricated wires show a narrow distribution range of 100–120 nm.

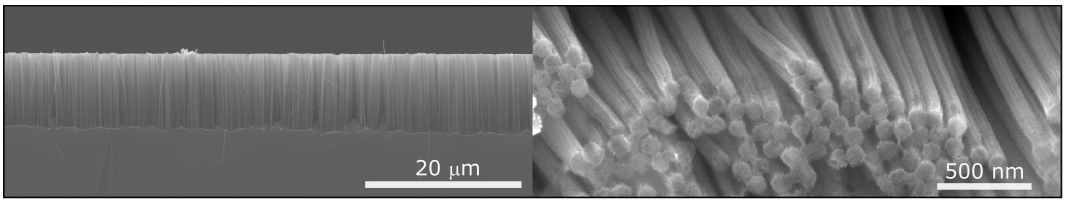

Figure 2. Scanning electron micrograph of the p-type heavily doped Si nanowire (P^+), fabricated via colloidal lithography as described in the experimental section.

In the present study, we have focused the investigation on the structural properties of the Si NWs, with different doping type and doping level looking at the modulation of the electronic properties of the selected wires. The list of fabricated samples using different doping type and level as well as etching electrolytic solutions is shown in Table 1.

Table 1. List of samples fabricated using Si wafers of different doping type and level by MAcE [15], in catalytic solutions with different ratio.

Sample Name	Doping Type	Doping Concentration (cm^{-3})	Etching Time	Electrolyte Ratio ($HF:H_2O_2:H_2O$)
p	B	10^{15}	6′	2 : 1 : 3
p^+	B	10^{18}	6′	2 : 1 : 3
p_0	B	10^{15}	6′	2 : 3 : 1
n^+	P	10^{18}	6′	2 : 1 : 3
n	P	10^{15}	6′	2 : 1 : 3

3.1. X-Ray Absorption Spectroscopy

X-ray absorption spectra of different Si NWs are compared in Figure 3. The measurements were performed in Total Electron Yield (TEY) mode collecting the photo-emitted drain current of the exposed sample surface to the beam with an estimated mean probing depth in the range of 2 and 10 nm. The measurements were performed in two stages. First, the spectra of the freshly fabricated nanowires were acquired and then the samples were moved to the preparation chamber attached to the experimental chamber of the beam-line and were subject to argon sputtering steps in order to have bulk structural information in addition to that from the surface.

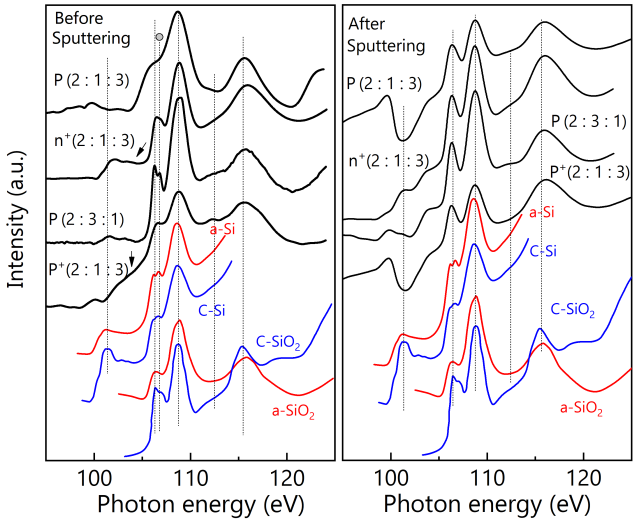

Figure 3. X-ray absorption of Si NWs fabricated by MAcE process [15], with different doping type (p and n) and doping level (p^+, n^+: 10^{18}; p, n: 10^{15}). Left panel: Si–L edge of fresh synthesized silicon nanowires. Right panel: Si–L edge of nanowires after three hours of sputtering. The reference spectra of c-Si, a-Si are taken from Ref. [22] and the c-SiO_2 and a-SiO_2 from Ref. [23].

The Si–L edge spectra of the as-fabricated samples of three doping type and level as well as one etched in a distinct solution concentration (see Table 1) are shown in Figure 3. The samples are Si NWs: highly boron doped (p+: 10^{18} at./cm^3); low boron doped (p: 10^{15} at./cm^3); highly phosphorous doped Si, etched in a 2:1:3 ratio of the etching solution of $HF:H_2O_2:H_2O$ (H_2O_2, being oxidizing agent and HF the etching agent) and low boron doped Si etched in a 2:3:1 ratio of the etching solution of $HF:H_2O_2:H_2O$. The spectra show main features at around 100 eV, 105.6 eV, 108.1 eV, 112.4 eV and around 115 eV corresponding to the a1(3s), t2(3p), e(ϵd) and t2+e(ϵd) respectively, corresponding to 3s, 2p and 3d like excitations of silicon and silicon oxide (e.g., SiO_2). Comparison of the spectra with the reference amorphous and crystalline silicon and silicon dioxide, it can be clearly observed that all samples show small edges related to the elemental silicon at around 100 eV, apart from the highly n-type doped sample that exhibits a higher ratio of the crystalline Si with an additional damped extended feature at around 104.4 eV (shown by arrow) which can be correlated with the spin-orbit splitting of the core excitation state of the oxide in the range of 104 eV to 106 eV [24,25]. However,

spectra are dominated by silicon oxide features and are characterized by small changes due to doping type and to the catalytic solution.

The *p*-doped samples, show the occurrence of a higher amorphization due to a large charge transfer and a sizeable broadening, in agreement with the higher etching rate. On the other hand, samples produced with the *n*-doped substrate show structures closer to the crystalline SiO_2. Moreover, the sample synthesized using a higher oxidizing agent ratio shows a peak splitting at around 107 eV (shown by circle), which can be assigned to either the formation of the SiO_2 (2p) or to the presence of other oxidation states. This fact is in agreement with the lack of the spin-orbit splitting feature in this sample, due to the distribution of the oxide stoichiometry that determines the smoothing of the spin-orbit splitting feature [23,24,26]. The Si–L edge spectra of the samples after three hours of Ar sputtering (at 600 μA, corresponding to the removal of 3–4 nm of top layers) are shown in the Figure 3b. The emergence of the spin-orbit splitting feature, being damped to the disordered superficial stoichiometry on the sample surface, is clearly visible in all the spectra. All the samples show a relatively similar silicon oxide formation ratio. The visible deep in the *p*-type Si NWs are related to the internal resonant absorption in disordered Si nano-crystallites [27]. However, the *p*-type doped samples with the lower ratio of etching solution (i.e., p^+) and *p*, see Table 1) show a relatively intense deep at the Si edge which might indicate higher crystalline Si content, compared to the p-type sample etched in the higher oxidizing agent solution (i.e., p_0). This agrees with higher oxidation rate via this solution and higher porosity of samples, as reported previously [15]. Furthermore, the n-type sample shows a relatively consistent features with its surface counterpart, though with a slight shift of the Si edge. This shift can be due to the formation of smaller silicon nanostructures which can result in a shift of the excitation edge of the XAS features due to the spatial confinement within the nanostructure [24].

Finally, the oxygen K-edge, shows main SiO_2 features in all samples prior to the sputtering (Figure 4a) and after the sputtering (Figure 4b). However, prior to the sputtering all the spectra show a broadening due to the presence of small amount of other oxides. Furthermore, due to the larger probing depth at the oxygen K-edge (∼5 nm) compared to Si–L edge (∼2 nm), the oxygen spectra can have traces of the features before sputtering. The sample fabricated with higher oxidant agent ratio (i.e., p_0, see Table 1), clearly shows the presence of a second component (labeled by *) in agreement with the splitting of the Si–L edge *p* excitation component of other oxidation states. The oxide component of the bulk remains relatively similar in all samples as shown by the O K-edge spectra collected after three hours of sputtering (Figure 4b) that indicate extension of the oxide layer beyond the sputtered layer thickness and the O K-edge TEY MPD (∼5 nm). For SiO_2 a small shoulder is usually observed around 533 eV which is very small in our case. This feature is damped due to presence of the amorphous silicon dioxide or by the presence of the other oxide stoichiometry (i.e., SiO_x).

3.2. Raman Spectroscopy

The Raman spectra of selected samples, synthesized with different doping types and levels, using similar etching solution ratio along with the bulk silicon reference are shown in Figure 5. Spectra evidence mainly a prominent peak between 500 and 520 cm^{-1} with a significant down-shift of the first-order optical phonon of the crystalline bulk Si. The down-shift observable in these samples can be attributed to the decrease of silicon crystallite size (the inner part of remnant Si units of nanowire maintaining the crystalline Si lattice). This is due to the relaxation of momentum conservation for which the Raman active modes will not be limited to the center of the Brillouin zone. Hence, smaller is the crystalline grain, larger is the frequency shifts and more asymmetric and broader the peak becomes [28]. The downshifts observed in our spectra, suggest the presence of larger Si structures in p-type NWs and smaller one in n-type NWs, in agreement with XAS results, discussed in the previous section.

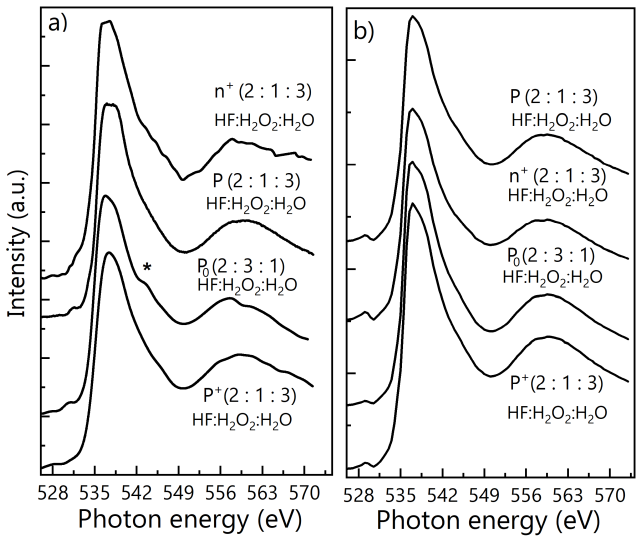

Figure 4. X-ray absorption of Si NWs fabricated by MAcE process, with different doping type and doping level (see Table 1). (**a**) O K-edge of as-fabricated nanowires. (**b**) O K-edge of sputtered nanowires.

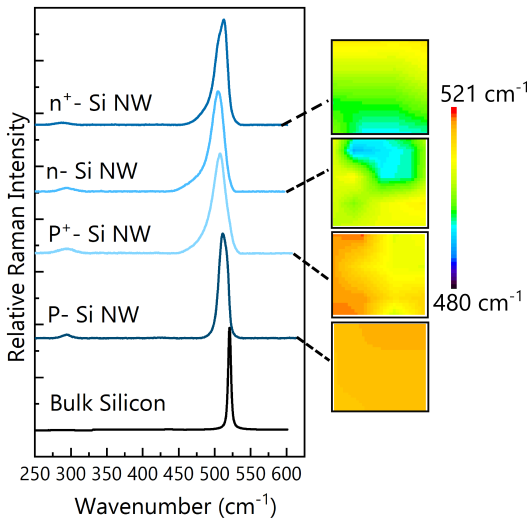

Figure 5. Raman spectra of Si NWs with different doping type and level, fabricated by the MAcE process using the etching solution of the HF:H_2O_2:H_2O with 2:1:3 ratio. For each sample, a relative Raman map of the down-shift of the Si first-order optical mode have been collected, within an area of 10×10 µm^2.

Except for the low *p*-doped sample (*p*), all the other Raman spectra evidence broad features between 476 cm^{-1} and 484 cm^{-1}. These can be correlated either to the quantum confinement in the inner structure of the wires or the presence of structural defects such as amorphization or disorder, which was also detectable in a certain amount in the XAS spectra and was also pointed out by previous studies [29–31]. Furthermore, the additional feature appearing at $\sim$ 300 cm^{-1} with relatively similar intensities, due to the scattering of two transverse acoustic (2TA) phonons, is also clearly visible [28,31]. To evaluate the relative distribution of the Si crystallite dimensions in distinct samples, Raman mappings of the down-shift of the first-order optical mode have been carried out, within an area 10×10 µm^2, pointing out a maximum value in the low level *n*-type doped sample.

3.3. Charge Carrier Transport

Electronic transport measurements were performed on two p-type silicon samples with two different oxidation agent to acid ratio (α = HF/H_2O_2 = 2 and 0.5 respectively), hence, with different levels of crystallinity (see XAS and Raman analysis).

To perform the measurement, wires were mechanically removed from the substrate and dispersed onto the surface of a SiO_2 wafer, on which a patterned layout of metal contacts was previously deposited. Investigated Si NWs, have a typical length of about 1.7 μm and a lateral size of $\sim$100 nm. They were contacted using Pt (see Figure 6a) by a focused ion beam (FIB) apparatus (see Ref [32]).

Selected I-V characteristics of one of the wires (p, $\alpha = 2$) in the temperature range of 10–300 K are shown in Figure 6b. The other wires show similar behaviors. The results clearly indicate a nonlinear thermally activated trend in the measured I-V characteristics, becoming linear near room temperature. To investigate the conduction mechanism in these wires, a resistivity measurements were carried out at a medium bias of 0.5 V. In both cases, the Arrhenius plot of the resistivity (see Figure 7a,b) reveals a continuous change of the activation energy, suggesting the existence of distinct conduction mechanisms in different temperature ranges. A detailed analysis of the resistivity trend in sample with lower crystalline Si component, revealed two different conduction regions. From 300 K down to 40 K, the resistivity shows a weak temperature dependence, with activation energies $\leq$20 meV. Below 40 K, the conduction becomes almost temperature independent, with an activation energy as low as $\simeq$ 3 meV. These values of the activation energies in the low temperature range usually suggest thermally activated hopping mechanisms [33]. The hopping in our sample was confirmed using the procedure suggested in Ref. [18], considering a general resistance increment as a function of temperature expressed as

$$R_i = C_i T^{bi} R_0 \exp\left[(\frac{T^{*i}}{T})^{m_i} \right] \tag{1}$$

in which C_i, b_i, T^{*i} and m_i are constant parameters with experimentally determined values.

Considering the temperature dependence of the resistivity in different regions, i, based on the activation energies, the corresponding m_i values indicating distinct conduction mechanism can be obtained from

$$\ln\left[T^{-1} \frac{d(\ln R)}{d(T^{-1})} \right] = B_i - m_i \ln(T_i) \tag{2}$$

where B_i is an experimentally determined constant parameter. Hence, the temperature dependence of the conduction mechanism in the nanostructure relates to the so-called reduced activation energy defined as

$$w = \ln\left[T^{-1} \frac{d(\ln R)}{d(T^{-1})} \right] \tag{3}$$

Analysis of w vs $\ln T$ behavior, on the sample with $\alpha = 0.5$, shows two distinctive regions with $m = 0.24$ below $\sim$ 40 K and $m = -0.96$ between 40 K and 300 K (Figure 7c). The $m = 0.24$ is an indicator of the well-known Mott's variable range hopping (VRH) conduction. Considering a constant density of state at Fermi level, which occurs in our sample below $T \approx 40$ K [34,35], the T^{*i}, in the reduced activation energy limit, assumes the form $T^* = 16/k_B N_a \alpha$, where N_a is the DOS at ϵ_F; k_B the Boltzmann constant and $1/\alpha$ is the localization length of charge carriers. Our analysis results in $T^* \simeq 2.4 \times 10^4$ K while assuming a localization length of $1/\alpha \approx 1$ nm [36] and the density of states (DOS) of the system is $N_a \approx 10^{21}$ eV^{-1}cm^{-3}. On the other hand, above 40 K, the activation energy shows a dependence with $m = -0.96$, for the whole temperature range up to 300 K. This value is in excellent agreement with $m = -1$ expected for the non-correlated transfer of the charge carriers among localized sites through a rectangular and thermally vibrating barrier (i.e., Berthelot tunneling). The model assumes that there exists a sufficiently dense network of identical centers and that the only parameter limiting the tunneling of carriers among centers is the barrier width. This last can be affected by thermal expansion, altering the equilibrium separation of the sites and through the

amplitude of the site's thermal oscillations, which changes the overlap degree. Considering a negligible thermal expansion [37], the thermal oscillation of the sites induces a direct temperature dependence of the carrier transport [37,38] as $R = R_0 \exp(T{T_B}^{-1})$, where T_B is a specific temperature related to the material and defined as

$$T_B = \frac{\hbar}{2\pi^2 {a_b}^2 {m_e}^* k_B} \tag{4}$$

with a_b the barrier width and m^* the electron effective mass [39]. Our analysis returns a value of T_B = 110 K in excellent agreement with the expected range of values for the Berthelot tunneling conduction [38,40].

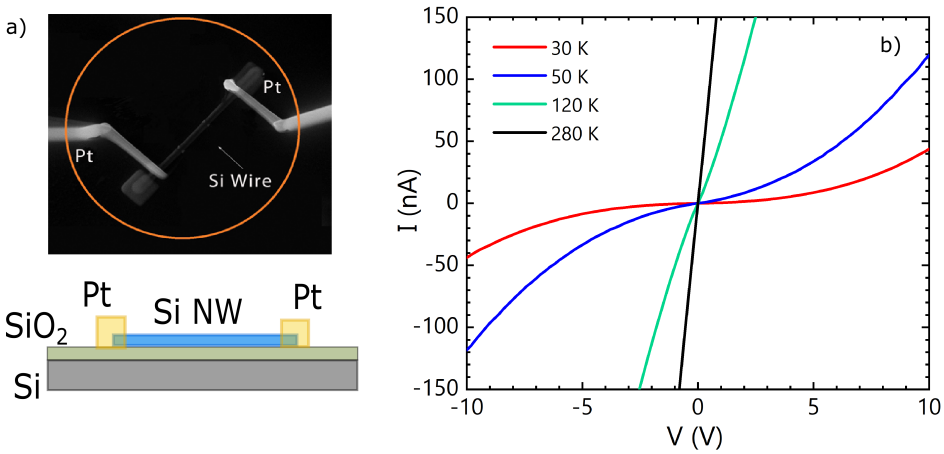

Figure 6. (**a**) SEM micrography of the contact geometry on a PS wire along with the schematic of the fabricated device. (**b**) I-V curves of the fabricated p-type Si nanowire at selected fixed temperatures. The current tends to increase approaching a linear behavior around room temperature.

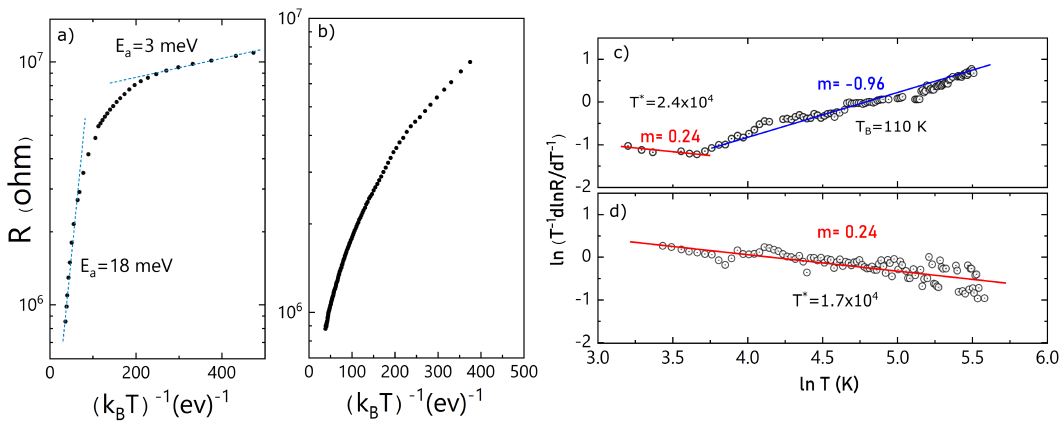

Figure 7. (**a**,**b**) Arrhenius plot of the nanowire with $\alpha = 0.5$ and $\alpha = 2$, respectively. (**c**,**d**) Plot of reduced activation energy $\ln[T^{-1}\frac{d(\ln R)}{d(T^{-1})}]$ vs $\ln T$ of the nanowire with $\alpha = 0.5$ and $\alpha = 2$, respectively. Circles are experimental data and lines are least square fitting. The values of the exponent m and corresponding temperatures are indicated in the plot.

A similar analysis on wires with $\alpha = 2$, in the similar temperature range, reveals a continuous change of the activation energy with a small temperature dependence (see Figure 7b). Using a similar approach, suggested by Zabrodskii, we found that the investigated Si NWs exhibit only a single slope in the temperature dependence, with a value $m = 0.27$ in agreement with the Mott's variable range hopping, though extending up to room temperature. The best fit of the resistivity data gives a $T^* = 1.7 \times 10^4$ K and a similar order of the density of states available for hopping ($N_a \sim 10^{21}$ eV^{-1}cm^{-3}).

The large DOS at ϵ_F observed in both samples are due to the large number of P_b centers, created by Si dangling bonds and B-atoms because of the huge internal surface inside NWs. These centers have low activation energies and are introduced in the silicon gap. On the other hand, the direct T dependence of the resistance observed in $\alpha = 0.5$ sample can be attributed to the isolated crystalline domains present within the structure of these wires [40] that induce tunneling among crystallites. These domains can be considered to be identical shallow centers separated by the amorphous/oxide barrier layer with a large localization length of the order of the center size. However, in the wires with $\alpha = 2$, these channels form connected percolative paths, hence, generating a persistent hopping conduction.

4. Conclusions

In this work, we have shown that the structural and electronic properties of Si NWs, fabricated via metal assisted etching, can be modulated by a suitable combination of doping type, doping level and etching recipes. Our results demonstrate the distinctive surface and bulk structure of the nanowires. The higher oxidizing agent in the etching recipe can significantly alter the crystallinity of the fabricated wires and may drive to distinct oxide stoichiometry. Furthermore, the p-type fabricated wires evidence higher crystallinity order, especially in the bulk. Raman investigation has detected significant down-shift of the first-order optical mode, corresponding to the decrease of the crystalline size dimensions in the nanowires. In particular, Si NWs with n-type doping show the smallest c-Si dimensions and higher geometrical confinement. The electronic transport properties of two p-type Si NWs, fabricated with two different etching recipes and hence a different level of crystallinity, show a significant density of state modulation, with a variable range hopping conduction. The charge carrier transport mechanisms observed in our NWs are the result of the geometry of the systems with a large internal surface and a significantly high density of states. In wires with higher oxidant ratio, separated conducting channels result in thermally activated tunnelling among them. On the other hand, in wires with lower oxidant ratio a continuous percolative conduction path is formed with a continuous variable range hopping of charge carriers. Although bulk porous silicon has already shown an improved sensitivity in many devices such as photo-detectors, when compared to bulk, the improved properties of these NWs and the possibility of controlling the dimension of the embedded Si structures, make these NWs promising candidates in many advanced opto-electronics applications.

Author Contributions: Conceptualization, S.J.R. and N.P. and R.G.; methodology, S.J.R. and R.G. and A.D.C. and A.D.; Data analysis, S.J.R. and A.D.C. and A.M. and N.P.; original draft preparation, S.J.R. and N.P. and A.M.; all authors have contributed equally in editing and reviewing the final draft. All authors have read and agreed to the published version of the manuscript.

Funding: This research received no external funding.

Conflicts of Interest: The authors declare that they have no conflict of interest.

References

1. Canham, L.T. Silicon quantum wire array fabrication by electrochemical and chemical dissolution of wafers. *Appl. Phys. Lett.* **1990**, *57*, 1046–1048.
2. Kang, Z.; Tsang, C.; Wong, N.; Zhang, Z.; Lee, S. Silicon Quantum Dots: A General Photocatalyst for Reduction, Decomposition, and Selective Oxidation Reactions. *J. Am. Chem. Soc.* **2007**, *129*, 12090–12091.
3. Pavesi, L.; Dal Negro, L.; Mazzoleni, C.; Franzo, G.; Priolo, F. Optical gain in silicon nanocrystals. *Nature* **2000**, *408*, 440–444.
4. D'Elia, A.; Cepek, C.; de Simone, M.; Macis, S.; Belec, B.; Fanetti, M.; Piseri, P.; Marcelli, A.; Coreno, M. Interplay among work function, electronic structure and stoichiometry in nanostructured VO x films. *Phys. Chem. Chem. Phys.* **2020**, *22*, 6282–6290, doi:10.1039/D0CP00216J.
5. Lehmann, V.; Gosele, U. Porous silicon formation: A quantum wire effect. *Appl. Phys. Lett.* **1991**, *58*, 856–858.
6. Borini, S.; Boarino, L.; Amato, G. Coulomb blockade tuned by NO2 molecules in nanostructured silicon. *Adv. Mater.* **2006**, doi:10.1002/adma.200600198.

7. Loni, A.; Defforge, T.; Caffull, E.; Gautier, G.; Canham, L. Porous silicon fabrication by anodisation: Progress towards the realisation of layers and powders with high surface area and micropore content. *Microporous Mesoporous Mater.* **2015**, *213*, 188–191.
8. Carturan, S.; Maggioni, G.; Rezvani, S.; Gunnella, R.; Pinto, N.; Gelain, M.; Napoli, D. Wet chemical treatments of high purity Ge crystals for γ-ray detectors: Surface structure, passivation capabilities and air stability. *Mater. Chem. Phys.* **2015**, *161*, 116–122, doi:10.1016/j.matchemphys.2015.05.022.
9. Deng, M.T.; Yu, C.L.; Huang, G.Y.; Larsson, M.; Caroff, P.; Xu, H.Q. Anomalous zero-bias conductance peak in a Nb-InSb nanowire-Nb hybrid device. *Nano Lett.* **2012**, doi:10.1021/nl303758w.
10. Nilsson, H.A.; Samuelsson, P.; Caroff, P.; Xu, H.Q. Supercurrent and Multiple Andreev Reflections in an InSb Nanowire Josephson Junction. *Nano Lett.* **2012**, *12*, 228–233, doi:10.1021/nl203380w.
11. Pasqualini, M.; Calcaterra, S.; Maroni, F.; Rezvani, S.; Cicco, A.D.; Alexander, S.; Rajantie, H.; Tossici, R.; Nobili, F. Electrochemical and spectroscopic characterization of an alumina-coated $LiMn_2O_4$ cathode with enhanced interfacial stability. *Electrochim. Acta* **2017**, *258*, 175–181, doi:10.1016/j.electacta.2017.10.115.
12. Rezvani, S.; Pasqualini, M.; Witkowska, A.; Gunnella, R.; Birrozzi, A.; Minicucci, M.; Rajantie, H.; Copley, M.; Nobili, F.; Cicco, A.D. Binder-induced surface structure evolution effects on Li-ion battery performance. *Appl. Surf. Sci.* **2018**, *435*, 1029–1036, doi:10.1016/j.apsusc.2017.10.195.
13. Pinto, N.; Rezvani, S.J.; Perali, A.; Flammia, L.; Milošević, M.V.; Fretto, M.; Cassiago, C.; De Leo, N. Dimensional crossover and incipient quantum size effects in superconducting niobium nanofilms. *Sci. Rep.* **2018**, *8*, 4710, doi:10.1038/s41598-018-22983-6.
14. Rezvani, S.J.; Gioacchino, D.D.; Gatti, C.; Ligi, C.; Guidi, M.C.; Cibella, S.; Fretto, M.; Poccia, N.; Lupi, S.; Marcelli, A. Proximity Array Device: A Novel Photon Detector Working in Long Wavelengths. *Condens. Matter* **2020**, *5*, 33.
15. Rezvani, S.J.; Gunnella, R.; Neilson, D.; Boarino, L.; Croin, L.; Aprile, G.; Fretto, M.; Rizzi, P.; Antonioli, D.; Pinto, N. Effect of carrier tunneling on the structure of Si nanowires fabricated by metal assisted etching. *Nanotechnology* **2016**, doi:10.1088/0957-4484/27/34/345301.
16. Rezvani, S.J.; Pinto, N.; Boarino, L. Rapid formation of single crystalline Ge nanowires by anodic metal assisted etching. *CrystEngComm* **2016**, *18*, 7843–7848, doi:10.1039/C6CE01598K.
17. Wagner, R.S.; Ellis, W.C. Vapor-Liquid-Solid Mechanism of Single Crystal Growth. *Appl. Phys. Lett.* **1964**, *4*, 89.
18. Pinto, N.; Rezvani, S.J.; Favre, L.; Berbezier, I.; Fretto, M.; Boarino, L. Geometrically induced electron-electron interaction in semiconductor nanowires. *Appl. Phys. Lett.* **2016**, doi:10.1063/1.4962893.
19. Rezvani, S.J.; Pinto, N.; Boarino, L.; Celegato, F.; Favre, L.; Berbezier, I. Diffusion induced effects on geometry of Ge nanowires. *Nanoscale* **2014**, *6*, 7469–7473, doi:10.1039/C4NR01084A.
20. Rezvani, S.J.; Favre, L.; Celegato, F.; Boarino, L.; Berbezier, I.; Pinto, N. Supersaturation state effect in diffusion induced Ge nanowires growth at high temperatures. *J. Cryst. Growth* **2016**, doi:10.1016/j.jcrysgro.2015.11.029.
21. BEAR Beamline, IOM-CNR. Available online: https://www.elettra.trieste.it/it/lightsources/elettra/elettra-beamlines/bear/bear.html (accessed on 15 July 2018).
22. Turishchev, S.Y.; Parinova, E.V.; Pisliaruk, A.K.; Koyuda, D.A.; Yermukhamed, D.; Ming, T.; Ovsyannikov, R.; Smirnov, D.; Makarova, A.; Sivakov, V. Surface deep profile synchrotron studies of mechanically modified top-down silicon nanowires array using ultrasoft X-ray absorption near edge structure spectroscopy. *Sci. Rep.* **2019**, *9*, 8066, doi:10.1038/s41598-019-44555-y.
23. Li, D.; Bancroft, G.M.; Kasrai, M.; Fleet, M.; Secco, R.; Feng, X.; Tang, K.; Yang, B.X. X-ray absorption spectroscopy of silicon dioxide (SiO2) polymorphs: the structural characterization of opal. *Am. Mineral.* **1994**, *79*, 622–632.
24. Harp, G.R.; Han, Z.L.; Tonner, B.P. Spatially-resolved X-ray Absorption Near-edge Spectroscopy of Silicon in Thin Silicon-oxide Films. *Phys. Scr.* **1990**, doi:10.1088/0031-8949/1990/T31/003.
25. Himpsel, F.J.; McFeely, F.R.; Taleb-Ibrahimi, A.; Yarmoff, J.A.; Hollinger, G. Microscopic structure of the SiO2/Si interface. *Phys. Rev. B* **1988**, *38*, 6084–6096, doi:10.1103/PhysRevB.38.6084.
26. Harp, G.R.; Han, Z.L.; Tonner, B.P. X-ray absorption near edge structures of intermediate oxidation states of silicon in silicon oxides during thermal desorption. *J. Vac. Sci. Technol. A Vac. Surf. Films* **1990**, doi:10.1116/1.576737.

27. Turishchev, S.; Terekhov, V.; Parinova, E.; Korolik, O.; Mazanik, A.; Fedotov, A. Surface modification and oxidation of Si wafers after low energy plasma treatment in hydrogen, helium and argon. *Mater. Sci. Semicond. Process.* **2013**, *16*, 1377–1381, doi:10.1016/j.mssp.2013.04.020.
28. Li, B.; Yu, D.; Zhang, S.L. Raman spectral study of silicon nanowires. *Phys. Rev. B* **1999**, *59*, 1645–1648, doi:10.1103/PhysRevB.59.1645.
29. Siu, G.G.; Wu, X.L.; Gu, Y.; Bao, X.M. Ultraviolet and blue emission from crystalline SiO2 coated with LiNbO3 and LiTaO3. *Appl. Phys. Lett.* **1999**, *74*, 1812–1814, , doi:10.1063/1.123094.
30. Khorasaninejad, M.; Walia, J.; Saini, S.S. Enhanced first-order Raman scattering from arrays of vertical silicon nanowires. *Nanotechnology* **2012**, *23*, 275706, doi:10.1088/0957-4484/23/27/275706.
31. Zhang, S.; Wang, X.; Ho, K.; Li, J.; Diao, P.; Cai, S. Raman spectra in a broad frequency region of p type porous silicon. *J. Appl. Phys.* **1994**, *76*, 3016–3019, , doi:10.1063/1.357504.
32. D'Ortenzi, L.; Monsù, R.; Cara, E.; Fretto, M.; Kara, S.; Rezvani, S.J.; Boarino, L. Electrical Contacts on Silicon Nanowires Produced by Metal-Assisted Etching: A Comparative Approach. *Nanoscale Res. Lett.* **2016**, *11*, 468, doi:10.1186/s11671-016-1689-x.
33. Zabrodskii, A. Electrical conductivity of heavily doped compensated n-type germanium produced by neutron doping. *Sov. Phys. Semicond.* **1980**, *14*, 670–676.
34. Mathur, R.; Mehra, R.; Mathur, P.; Jain, V. Electron transport in porous silicon. *Thin Solid Film.* **1998**, *312*, 254–258.
35. Mott, S. *Conduction in Non-Crystalline Materials*; Oxford University Press: Oxford, UK, 1987.
36. Islam, M.N.; Islama, S.K.R.; Kumar, S. Mott and Efros-Shklovskii hopping conductions in porous silicon nanostructures. *Phys. E Low-Dimens. Syst. Nanostruct.* **2009**, *41*, 1025–1028.
37. Hurd, C. Quantum tunnelling and the temperature dependent DC conduction in low-conductivity semiconductors. *J. Phys. C Solid State Phys.* **1985**, *18*, 6487–6499.
38. Mares, J.; Kristofik, J.; Smid, V. Surface conductance in semi-insulating GaAs. *Semicond. Sci. Technol.* **1992**, *7*, 119.
39. Kapoor, M.; Singh, V.A.; Johri, G.K. Origin of the anomalous temperature dependence of luminescence in semiconductor nanocrystallites. *Phys. Rev. B* **2000**, *61*, 1941–1945, doi:10.1103/PhysRevB.61.1941.
40. Mehra, R.M.; Agarwal, V.; Singh, V.A.; Mathur, P.C. Unified model for the luminescence and transport data in self-supporting porous silicon. *J. Appl. Phys.* **1998**, *83*, 2235–2240.

© 2020 by the authors. Licensee MDPI, Basel, Switzerland. This article is an open access article distributed under the terms and conditions of the Creative Commons Attribution (CC BY) license (http://creativecommons.org/licenses/by/4.0/).